Vortex Generator Induced Flow in a High Re Boundary Layer

Velte, Clara Marika; Braud, C.; Coudert, S.; Foucaut, J.-M

Published in:
Journal of Physics: Conference Series (Online)

Link to article, DOI:
10.1088/1742-6596/555/1/012102

Publication date:
2014

Document Version
Publisher's PDF, also known as Version of record

Vortex Generator Induced Flow in a High Re Boundary Layer

2014 J. Phys.: Conf. Ser. 555 012102

(http://iopscience.iop.org/1742-6596/555/1/012102)

Vortex Generator Induced Flow in a High Re Boundary Layer

C M Velte[1], C Braud[2], S Coudert[2] and J-M Foucaut[3]

[1] Wind Energy Department, Technical University of Denmark, 2800 Kgs. Lyngby, Denmark
[2-3] Univ. Lille Nord de France F-59000 Lille, CNRS[2], EC Lille[3], Laboratoire de Mécanique de Lille (UMR 8107) Boulevard Paul Langevin, 59655 Villeneuve d'Ascq Cedex

E-mail: cmve@dtu.dk

Abstract. Stereoscopic Particle Image Velocimetry measurements have been conducted in cross-planes behind three different geometries of Vortex Generators (VGs) in a high Reynolds number boundary layer. The VGs have been mounted in a cascade producing counter-rotating vortices and the downstream flow development was examined. Three VG geometries were investigated: rectangular, triangular and cambered. The various VG geometries tested are seen to produce different impacts on the boundary layer flow. Helical symmetry of the generated vortices is confirmed for all investigated VG geometries in this high Reynolds number boundary layer. From the parameters resulting from this analysis, it is observed at the most upstream measurement position that the rectangular and triangular VGs produce vortices of similar size, strength and velocity induction whilst the cambered VGs produce smaller and weaker vortices. Studying the downstream development in the ensemble and spanwise averaged measurements, it is observed that the impact from the rectangular and triangular VGs differs. For the rectangular VGs, self-similarity in the streamwise component was confirmed.

1. Introduction

Vortex Generators (VGs) are commonly employed on wind turbine blades to transfer high momentum fluid closer to the wall and thereby control separation. This can improve the energy output and loads and thus allow the use of more slender blades, which in turn facilitates up-scaling of the turbine. It is therefore of vital importance to better understand the flow generated by these vanes.

This has been attempted in various works, but few have so far been able to investigate the instantaneous vortex structures due to the lack of available techniques. This was eventually possible with the advent of Particle Image Velocimetry (PIV), which can provide repeated instantaneous flow realizations throughout a plane or even a volume. Stereoscopic PIV (SPIV) is an extended version of two-component PIV that provides all three velocity components (as opposed to two components for regular PIV). SPIV has been applied on vortex generators on a bump in a high Reynolds number boundary layer that would otherwise be on the verge of separation [1]. This parametric study optimized the VGs for the current geometry using hot-film shear-stress probes and the optimal flow was characterized with SPIV.

Given a similar geometrical arrangement at low Reynolds numbers (counter-rotating actuators, spanwise spacing, vane height etc.), it has been shown that the generated vortex possesses helical symmetry [2]. Together with a Batchelor vortex model this allows the generated flow to be described by merely four parameters: vortex core radius ε, circulation Γ, convection velocity u_0 and helical pitch l, leaving no restrictions on the shape of the vortex core. This model was further expanded to include the downstream vortex development using self-similarity analysis [3] in a low Reynolds number flow

with a negligible streamwise pressure gradient. In practice, this model can significantly reduce costly and time consuming parametric studies on vortex generators in the future.

To confirm this model at more applicable conditions (i.e., higher Reynolds numbers), a measurement campaign was conducted in a unique wind tunnel located in Lille, France, to more closely mimic the flow conditions of a real wind turbine blade. A sketch of the wind tunnel can be seen in Figure 1. Also shown is a measured boundary layer profile (measured by hot-wire anemometry, c.f. http://lml.univ-lille1.fr/lml/?page=144&menu_curr_set=144) in wall coordinates (U^+, y^+) at different Reynolds numbers based on the momentum thickness (R_θ) to illustrate the fully developed turbulent boundary layer, where κ and c are the well-known constants of the log-law. The Laboratoire de Mécanique de Lille (LML) wind tunnel facility has been specially designed to study fully developed turbulent boundary layers at high Reynolds numbers. The 20 m long developing section allows a boundary layer thickness of about 30 cm [4]. The large scales of the boundary layer allow detailed studies of the physics of the vortices with good accuracy.

Three types of passive devices and their impact on the flow are compared qualitatively and quantitatively using the model: rectangular, triangular and cambered. Note that these measurements form an ideal basis for future computer flow simulations due to their high Reynolds number. This may facilitate parametric studies as well as studies of the impact of streamwise pressure gradients.

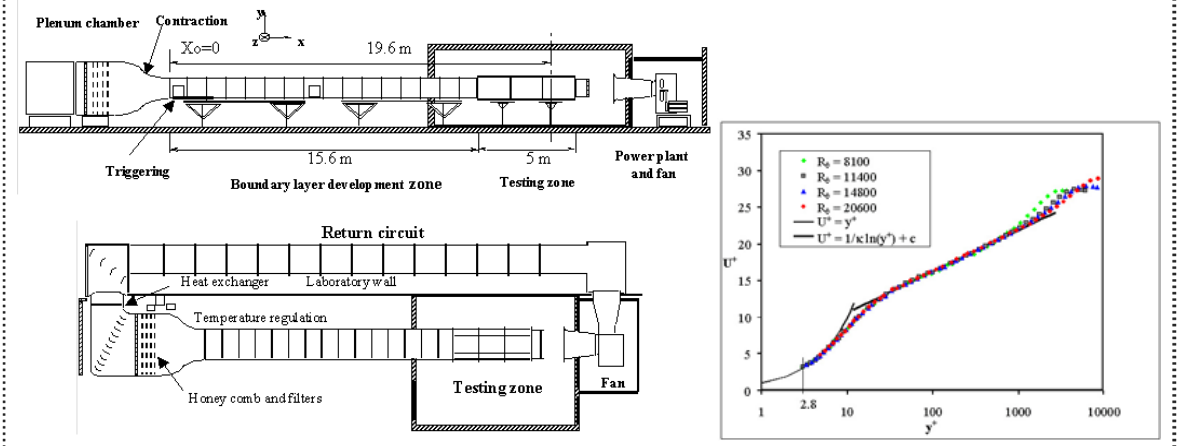

Figure 1. Side and top view of the LML boundary layer wind tunnel accompanied by boundary layer velocity profiles measured in the tunnel by hot-wire anemometry. Figure from http://lml.univ-lille1.fr/lml/?page=144&menu_curr_set=144.

2. Experimental setup

The Laboratoire de Mécanique de Lille (LML) wind tunnel facility has been specially designed to study fully developed turbulent boundary layer at high Reynolds number, see Figure 1. The boundary layer can develop over a section of length 20.6 m, where the last 5 m constitute the test section. In this most downstream region the boundary layer thickness increases merely 1 mm over 5 m length. The test section cross section is 2 x 1 m with windows on both sides. A cooling system can stabilize the temperature within a span of ±0.2°. The bulk velocity is continuously adjustable between 0-10 m/s.

In this wind tunnel, an experiment was performed to characterize vortices generated by specific vortex generators in the turbulent boundary layer. Three types of passive vortex generators and their downstream impact on the flow were investigated (see Figure 2):

- Rectangular
- Triangular
- Cambered

All of these were of height h = 60 mm and length $l_{VG} = 2h$. The cambered VGs were manufactured from the same type as the rectangular ones with a bending radius of 382 mm. Each respective configuration was mounted in a fashion producing a cascade of counter-rotating vortices with a spanwise period of λ/h = 6 and distance between trailing edges in a pair of L/h = 2.5 with a device angle β = 18° to the oncoming flow, see Figure 3.

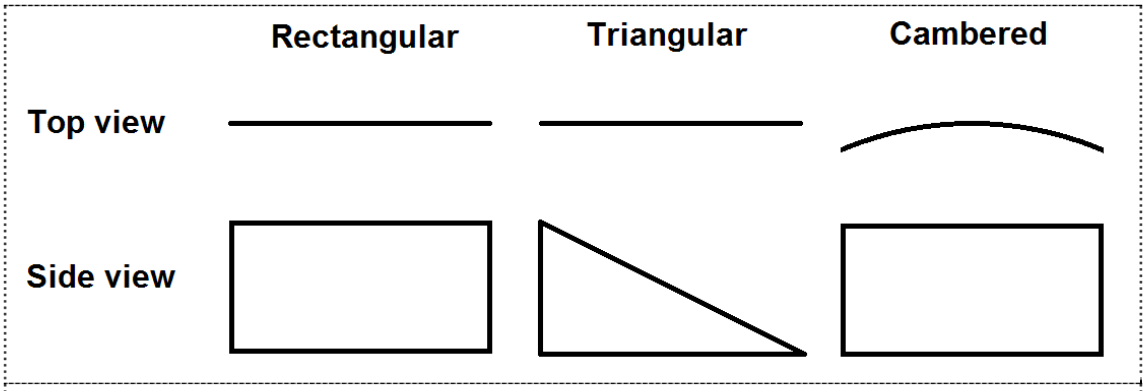

Figure 2. Investigated VG geometries, top and side views.

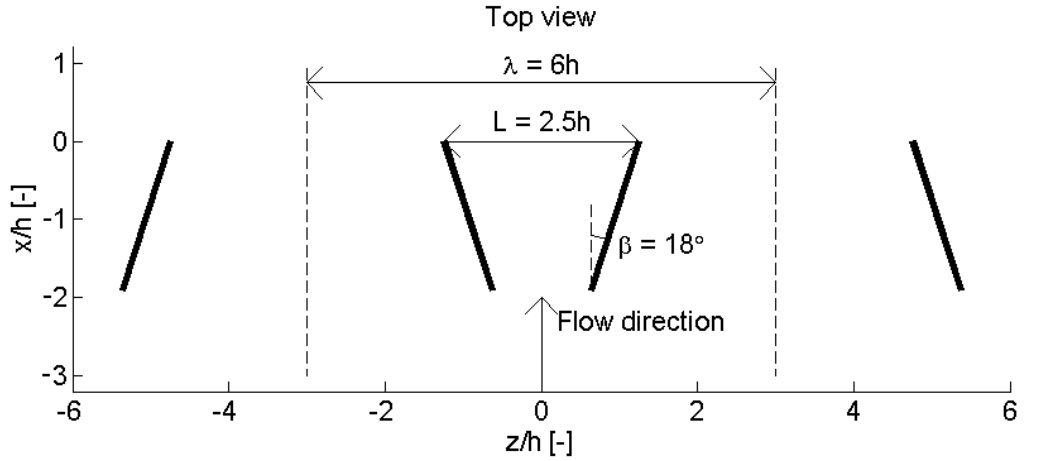

Figure 3. VG arrangement, top view. The parameters are the same as the optimal ones found in Godard and Stanislas [1].

A large field Stereoscopic Particle Image Velocimetry (SPIV) in a plane normal to the flow was used. The Reynolds number based on momentum thickness studied was 17.000. Figure 4 shows a sample velocity vector field realization produced by the triangular vanes. The axes are normalized by the boundary layer thickness δ. The vectors correspond to the instantaneous in-plane velocity components and the contour to the instantaneous streamwise (out of plane) velocity component.

Figure 5 shows a top view of the SPIV-setup. The PIV system was imaged with two Stereoscopic PIV systems in order to enlarge the field of view. Each system is based on two Hamamatsu 2k x 2k pixel cameras and micro Nikkon 105 mm lenses at f# 5.6. The field of view of each system is about 40 x 25 cm^2. Both systems were adjusted with a large overlap region in order to obtain, after merging, a final field of view of about 75 x 28 cm^2. These dimensions are comparable to the boundary layer

thickness in the wall normal direction and to about 5 integral scales in the spanwise direction. In that plane, the grid spacing is 2 mm which corresponds to 40 wall units.

The laser used was an Nd:YAG system with 2 cavities which is able to produce energy of 220 mJ per pulse at a frequency of 12 Hz. A mirror was positioned under the bottom glass in order to reflect the light in the wind tunnel and increase the light intensity. The beam waist was then located at the glass wall. Moreover each SPIV system was adjusted with respect to the Scheimpflug conditions [5]. The seeding consisted of Poly-Ethylene Glycol micron particles of size ~1 μm.

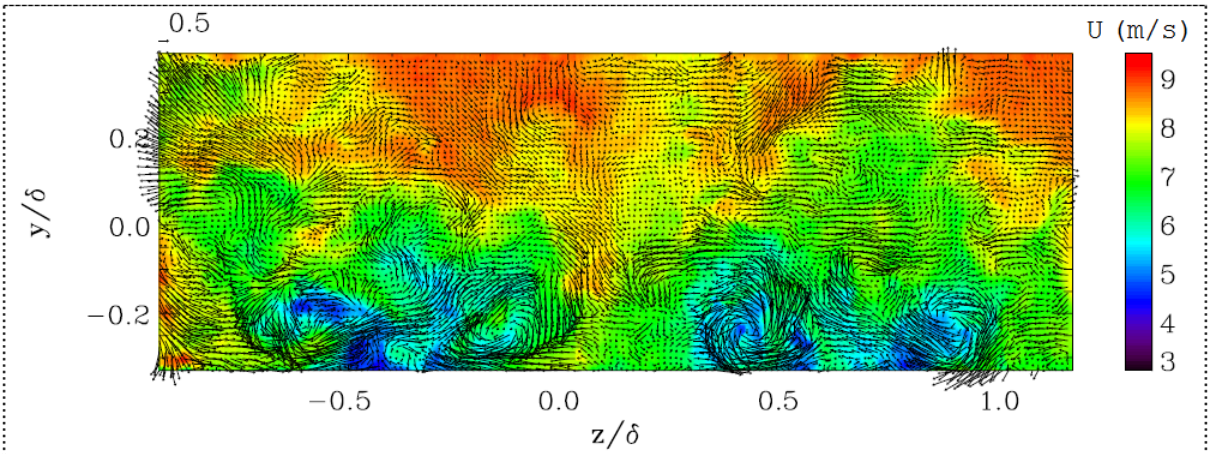

Figure 4. Example of instantaneous velocity field, x/h = 12. The axes are normalized by the boundary layer thickness δ.

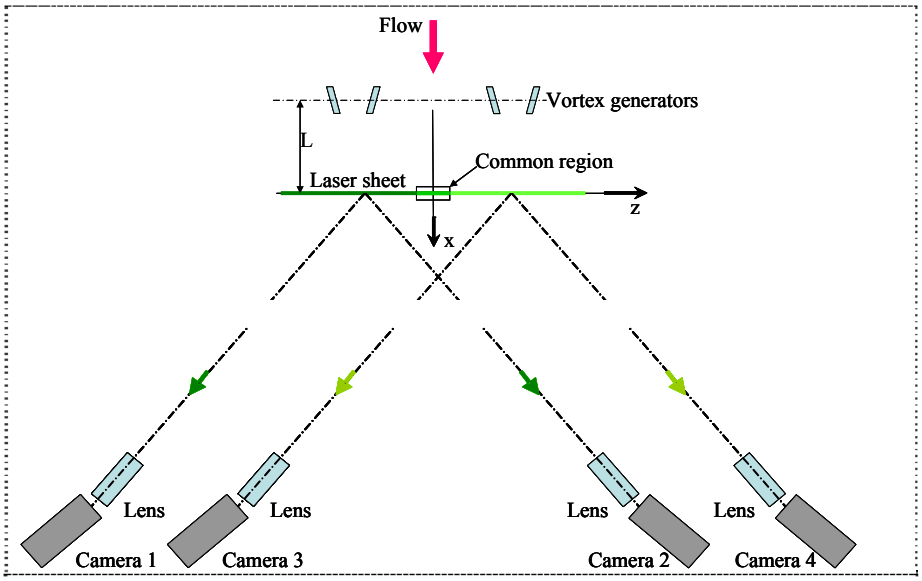

Figure 5. Experimental setup consisting of two Stereoscopic PIV systems.

The two light sheets (pulses) were slightly shifted in the streamwise direction, in order to optimize the dynamic range of the PIV. The shift is given by the mean velocity in the field

$$\Delta x = U\,\Delta t \tag{1}$$

of the order of 1.25 mm (for an estimated mean velocity) with a light sheet thickness of about 1 mm (corresponding to more than $6\sqrt{u^2}$ if imposing the time delay Δt) which allows a certain flexibility of the dynamics. Based on previous results obtained by hot wire anemometry, the local value of Δx can be estimated [6]. The PIV delay is 250 μs in order to optimize the dynamic range with a minimum of filtering and a maximum of displacement. The maximum mean displacement is then 10 px with a RMS of 0.8 px close to the wall.

The LML in-house PivLML code was used to process the images. In the present experiment, the self-correction process for both light sheets and for each SPIV system can be applied [7]. From the disparity map the location of each light sheet can be estimated. The distance between the two light sheets was observed to be about 1.2 mm, as expected. An angle of 0.15° between the light sheet and the calibration plane was also noted. This angle can be easily compensated by the self-correction process. For the stereoscopic reconstruction, the Soloff method was used [8]. The calibration was done using 3 planes located at 0 and ± 2 mm giving a calibrated volume depth of 4 mm. The calibration volume is then 4 mm by 750 mm, which with ease covers the illuminated particles. A more in-depth discussion of the accuracy of the measurements can be found in [6].

3. Model

The current model builds on the combination of two previous observations: the vortices (i) have helical symmetry and (ii) are self-similar. For practical reasons, only a brief description is given in the current text. For more detail, please see [2,3].

It has previously been shown that the generated vortices possess helical symmetry [2]. This means that the axial, u_ζ, and rotational, u_Θ, velocities are linearly related:

$$u_\zeta = u_0 - r\,u_\theta / l \tag{2}$$

(ζ,Θ,r) are the coordinates in a polar coordinate system (see Figure 6) of the longitudinal vortex where ζ is along the vortex center axis. u_0 is the vortex convection velocity, r the radial coordinate and l the helical pitch.

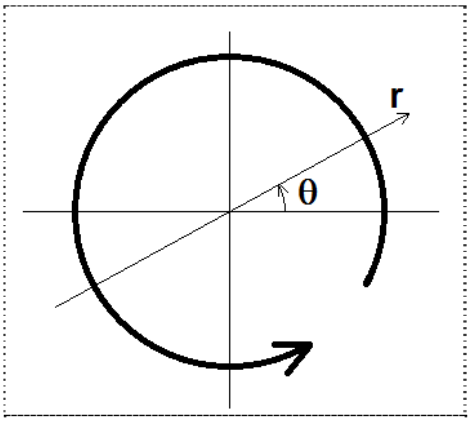

Figure 6. Polar coordinate system applied to the vortex core.

Together with the Batchelor vortex model

$$u_\theta(r,\theta,\zeta)=\frac{\Gamma(\zeta)}{2\pi r}\left[1-\exp\left(-\frac{r^2}{\varepsilon^2(\theta,\zeta)}\right)\right];\quad u_\zeta(r,\theta,\zeta)=u_0(\zeta)-\frac{\Gamma(\zeta)}{2\pi l(\theta,\zeta)}\left[1-\exp\left(-\frac{r^2}{\varepsilon^2(\theta,\zeta)}\right)\right] \quad (3)$$

this allows the generated flow to be described by merely four parameters: vortex core radius $\varepsilon(\Theta,\zeta)$, circulation $\Gamma(\zeta)$, convection velocity $u_0(\zeta)$ and helical pitch $l(\Theta,\zeta)$, leaving no restrictions on the shape of the vortex core. Further, all parameters are observed to vary linearly with downstream distance [3] (in a negligible streamwise pressure gradient boundary layer) and with vane angle [2].

This model was further expanded to include the downstream vortex development using self-similarity analysis [3] in a low Reynolds number flow with a negligible streamwise pressure gradient. Self-similarity is based on the idea of self-preservation across scales. This kind of analysis is commonly used on jets, but can conveniently be applied to wakes as well [9]. For the measured time-averaged far wake behavior it is posed that:

$$\frac{u_\zeta-u_0}{U_e-u_0}=fcn\left(\frac{r}{\varepsilon}\right) \quad (4)$$

where the vortex core radius $\varepsilon(\Theta,\zeta)$ is chosen as the characteristic width of the wake and U_e is the ambient streamwise velocity. Note that $\varepsilon=\varepsilon(\Theta,\zeta)$, $l=l(\Theta,\zeta)$ and $u_0=u_0(\zeta)$ are all functions of the vortex axial coordinate ζ. The nominator in the left hand side of the self-similarity relation (4) should also be compared to the velocity formulation (2), which has been confirmed to apply to the current flow [2]. A convenient scaling for the azimuthal velocity u_Θ is to normalize it by the maximum value of u_Θ. The self-similarity scaling variables used are indicated in Figure 7. From self-similarity of u_ζ and u_Θ, the model presented in [3] can be extended to include the downstream development (ζ-dependence) of the vortices. In practice, this model can significantly reduce costly and time consuming parametric studies on vortex generators in future studies.

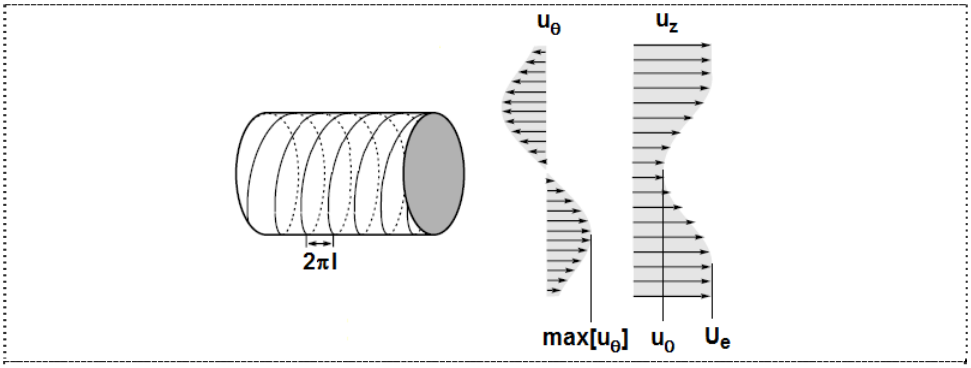

Figure 7. Principal sketch of the helical vortex core with helical vorticity lines (left) and the corresponding induced axial and rotational velocity fields (right). The self-similarity normalization parameters are indicated in the figure.

4. Results

In an attempt to mimic the flow conditions of a real wind turbine blade in order to confirm the model at more applicable conditions, a measurement campaign was conducted in the unique high Reynolds number boundary layer wind tunnel described in the experimental methods section (Figure 1).

The velocity profiles for the base flow and for each VG geometry (two to three positions each) are presented in Figure 8. Note that the downstream measurement positions may vary from case to case.

These profiles are obtained by ensemble averaging 500 realizations and then spanwise averaging across the field of view of the measurements. Already from this simple analysis, it is clear from the results that the impact of the various VG geometries on the flow differ from one another.

The streamwise flow is retarded, compared to the base flow, for all cases. This can be explained mainly due to the redistribution of energy to other velocity components (the rotational motion) and increased turbulence. Further, the initial wake profile grows and spreads away from the wall, as expected due to viscous dissipation and classical vortex theory. The rectangular vanes appear to have a larger effect on the flow further away from the wall than the triangular and cambered ones.

The vortices were then instead detected directly from the instantaneous snapshot vector fields obtained from the measurements. The detection was based on the minimum axial velocity and the swirl centre of the vortex. Subsequently, the coordinate system was transformed to polar with origo positioned at the vortex centre for each respective snapshot, see Figure 6. All realizations were then averaged with this common origo, so that the averaging was always carried out in the reference frame of the instantaneous vortex core. The following analysis will be based on data averaged in this fashion. Since the boundary layer is highly turbulent, the vortex cores are not always well distinguishable far downstream in the instantaneous flow and therefore the following analysis and comparison includes only the first position (3*h* downstream of the VG trailing edge).

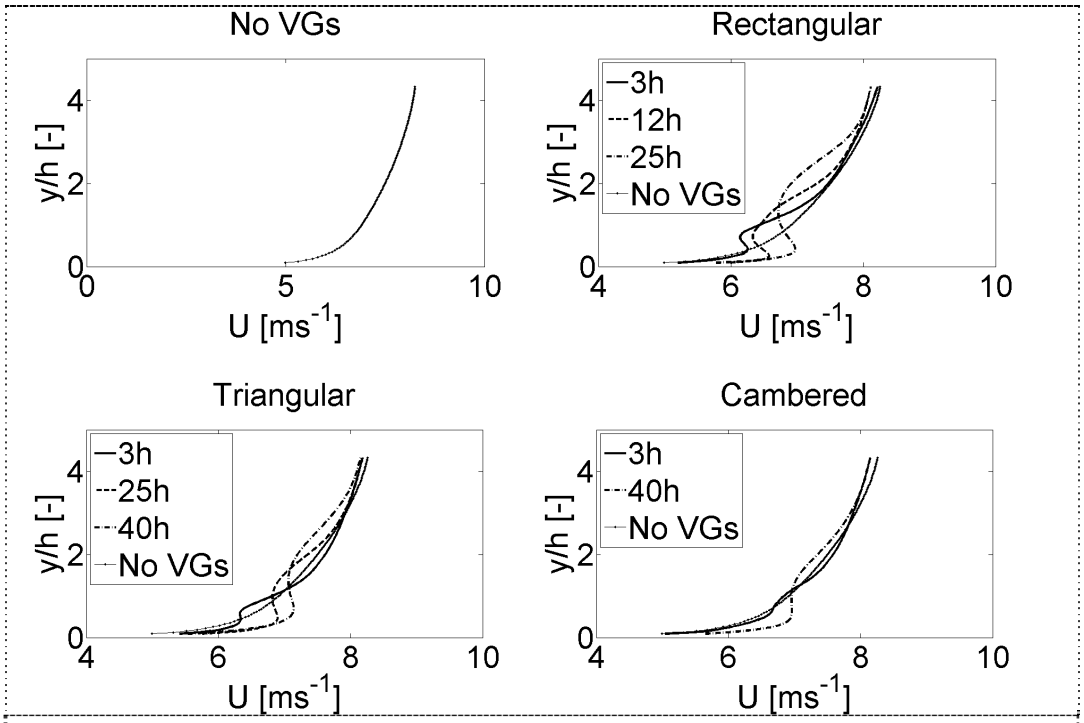

Figure 8. Averaged velocity profiles, comparison between base flow and the flow produced by different VG geometries.

The next step is to verify that the helical symmetry of the vortices, as reported e.g. in [2], remains intact at this higher Reynolds number. This is tested by matching of the left (u_z) and the right (u_0-ru_Θ/l) hand sides of the velocity formulation (2), which have been fitted using least-squares fitting for obtaining a value of the helical pitch, l. If there exists a value l that results in a collapse of the two curves, the vortex core obeys helical symmetry. Note that the remaining quantities in the velocity formulation can be obtained directly from the data. In Figure 9 this test has been performed for all three VG geometries and at various azimuthal angles Θ (as defined from the vortex core local

coordinate system in Figure 6) as indicated above each respective column. u_z are plotted as the black squares (□) and u_0-ru_θ/l is plotted as red circles (○).

It is clear that all VG geometries produce vortices that satisfy helical symmetry, even as close as x/h = 3 to the VG trailing edge. The helical parameters that result from the analysis are presented and compared for each VG geometry at 3h downstream of the VG. The circulation was obtained by path integration for higher accuracy than could be obtained through the Batchelor vortex model. Further, the vortex core radius ε was obtained from the azimuthal velocity component where the radius corresponds to its maximum value. Since these parameters are sufficient to describe the full vortex cores (at least in principle), they give an idea about the efficiency of each respective VG geometry.

All four helical parameters are presented for all three VG geometries in Figure 10. From the circulation diagram (Γ), it is apparent that the rectangular devices produce the strongest vortices, closely followed by the triangular ones. The cambered ones are only about half as efficient in the present configuration. A similar trend is seen in the vortex core size (ε), where the rectangular and triangular VGs produce larger structures, while the cambered one produces a smaller vortex core.

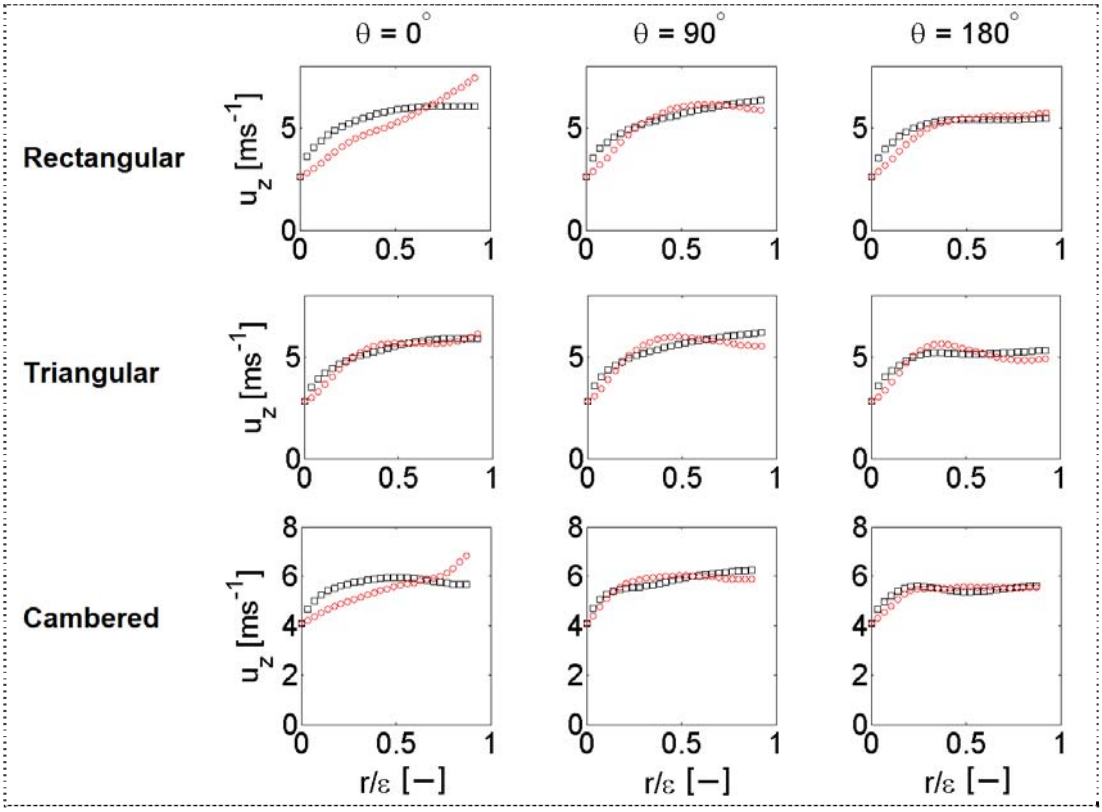

Figure 9. Validation of helical symmetry for each VG geometry, x/h = 3.

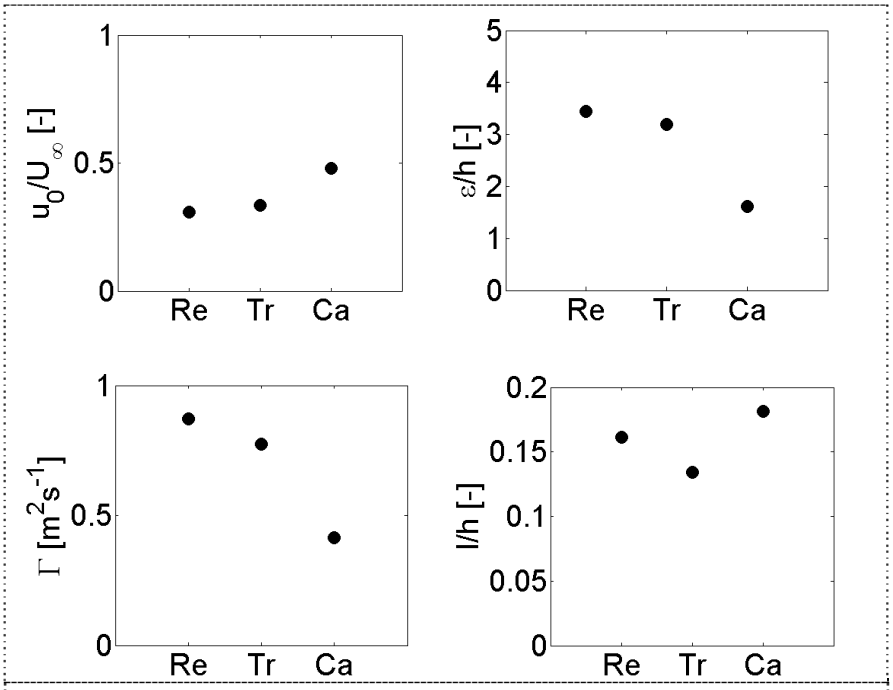

Figure 10. Helical parameters dependency on VG geometry, x/h = 3.

The relative differences are smaller in the convection velocity (u_0) and helical pitch (l), though the velocity profiles obtained from direct averaging shown in Figure 8 support these figures. The reduced axial velocity (the induction 'dip' seen in the streamwise profiles) is more distinct for the rectangular and triangular VGs in the near wake.

In the present measurements, only the rectangular devices provided satisfactory distinction of the vortex cores from the turbulent background flow to be located throughout the downstream positions. The self-similarity analysis is therefore based only on these data. Due to a perturbing secondary vortex on the one side of the primary vortex [2] (pp. 172-175), the analysis is only valid on the unperturbed side and therefore only these data are presented in Figure 11. Still, the similarity-scaled profiles display a nice collapse and thus the vortices have the property of self-similarity. The position closest to the VG ($3h$) deviates somewhat from the other two positions, which may be explained by the fact that this position lies within or at least very near the unstable forming region of the vortex, after which the vortex stabilizes [3].

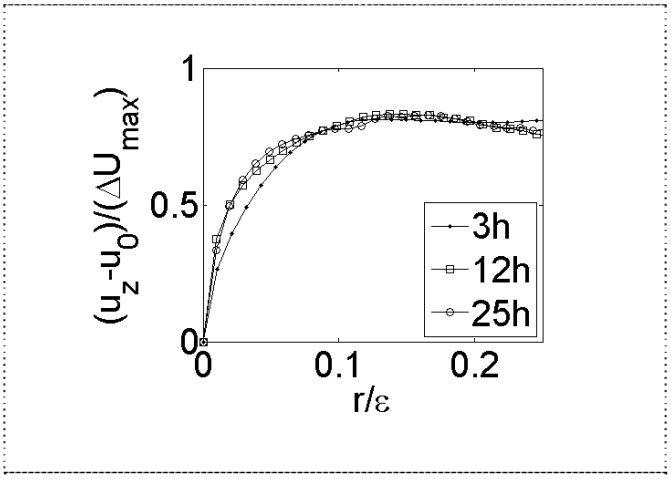

Figure 11. Self-similarity of the VG wake vortices in the downstream direction, rectangular devices.

5. Summary and conclusions

It is clear from the results that the choice of VG geometry can have distinguishable impact on the resulting flow. The criteria for helical symmetry were tested and confirmed on the present high Reynolds number boundary layer data. The analysis resulted in four parameters: vortex convection velocity, vortex core radius, circulation and helical pitch. Comparing these parameters for the three geometries at the measuring position closest to the VGs revealed that the rectangular and triangular devices have a quite similar impact there, as opposed to the cambered VGs which produced smaller (~50%) and weaker (~50%) vortices. Though similar at the most upstream position, the averaged velocity profiles reveal that the downstream flow development produced by the various VG geometries differs. This may be a concern of meandering or simply that the vortices have not yet fully developed at the early stage in the most upstream recorded position. This issue has practical importance due to the concern of parasitic drag from the VGs, which depends on the VG geometry, and should therefore be studied more in detail. Self-similarity of the vortices was tested and confirmed for the rectangular devices.

6. References

[1] Godard G and Stanislas M 2006 "Control of a decelerating boundary layer. Part 1: Optimization of passive vortex generators" *Aerosp. Sci. Tech.* **10**, 181-191.

[2] Velte C M, Hansen M O L H and Okulov V L 2009 "Helical structure of longitudinal vortices embedded in turbulent wall-bounded flow" *J. Fluid Mech.* **619**, 167-177.

[3] Velte C M 2012 "A vortex generator flow model based on self-similarity" *AIAA J.* accepted for publication.

[4] Carlier J and Stanislas M 2005 "Experimental study of eddy structures in a turbulent boundary layer using Particle Image Velocimetry" *J. Fluid Mech.* **535**, 143-188.

[5] Willert C 1997 "Stereoscopic digital particle image velocimetry for applications in wind tunnel flows" *Meas. Sci. Techn.* **8**, 1465-1479.

[6] Foucaut J M, Coudert S, Braud C and Velte C M 2012 "Large field SPIV in a spanwise plane of a high Reynolds number turbulent boundary layer with vortex generators to characterize streamwise vortices" *16th international symposium on applications of laser techniques to fluid mechanics*.

[7] Coudert S and Schon J P 2001 "Back-projection algorithm with misalignment corrections for 2D3C Stereoscopic PIV" *Meas. Sci. Techn.* **12**, 1371-1381.
[8] Soloff S, Adrian R and Liu Z-C 1997 "Distortion compensation for generalized particle image velocimetry" *Meas. Sci. Techn.* **8**, 1441-1454.
[9] White F M 1991 *Viscous Fluid Flow* 2nd ed., (New York: McGraw-Hill), pp. 470-481.

Acknowledgments
The work was supported through the International Campus on Safety and Inter modality in Transportation (CISIT) and the French Embassy grant N° 34/2011-CSU 8.2.1 as well as EUDP-2009-II-grant Journal number 64009-0279.